Accurate Star Centroid Detection for the Advanced Geosynchronous Radiation Imager of Fengyun-4A

HAOPENG ZHANG [1,2], **(Member, IEEE), YI SU** [1,2], **JIAN SHANG** [3], **LEI YANG** [3], **BOWEN CAI** [1,2], **CHENGBAO LIU** [3], **JING WANG** [3], **SHENGXIONG ZHOU** [4], **AND ZHIQING ZHANG** [3]

[1] Image Processing Center, School of Astronautics, Beihang University, Beijing 100191, China
[2] Beijing Key Laboratory of Digital Media, Beihang University, Beijing 100191, China
[3] National Satellite Meteorological Center, China Meteorological Administration, Beijing 100081, China
[4] Southwest Electronics and Telecommunication Technology Research Institute, Chengdu 610000, China

Corresponding authors: Jian Shang (shangjian@cma.gov.cn), Lei Yang (yangl@cma.gov.cn), Shengxiong Zhou (13136759@qq.com), and Zhiqing Zhang (zqzhang@cma.gov.cn)

ABSTRACT Star observation can be used for the image navigation of certain instruments aboard the three-axis stabilized geostationary satellites. How to extract the accurate star centroids in the observed star images is one of the key problems. In this paper, a high precision star centroid detection method is proposed for the advanced geosynchronous radiation imager (AGRI) of Fengyun-4A (FY-4A), the first experimental satellite of the new generation of Chinese geostationary meteorological satellites FY-4 series. Different from star sensors which are deliberately defocused with relatively large star spot, AGRI is focused for the purpose of earth observation, making it challenging to extract accurate star centroids. To solve the problem, we take the advantage of continuous observing and improve the precision of star centroiding by trajectory fitting and energy response curve fitting. Extensive experiments have been performed on simulated star images and the actual observation data of AGRI aboard FY-4A over ten months in-orbit tests. Experimental results show that the proposed method can accurately extract star centroids with the error less than 0.3 pixels, laying a solid foundation for image navigation of FY-4A.

INDEX TERMS Star centroiding, energy response curve, trajectory fitting, Fengyun-4A, geostationary satellite.

I. INTRODUCTION

The Chinese Fengyun (FY) meteorological satellite observing system is one of the main meteorological Earth observing systems in the world. It consists of both polar-orbiting and geostationary observational systems including a series of satellites. The odd numbers of FY denote the polar-orbiting satellite series (e.g. FY-1 and FY-3) and the even numbers denote the geostationary satellite series (e.g. FY-2 and FY-4) [1], [2]. During the past thirty years, Fengyun satellites have provided a large amount of observing data for the task of accurate understanding and forecasting of the weather, climate, environment and natural disasters in China and other areas. Launched on December 11, 2016, Fengyun-4A (FY-4A) is the first satellite of the new generation of Chinese geostationary meteorological satellites series Fengyun-4 (FY-4) [3]. As an experimental satellite, the objective of FY-4A is to show the improved capabilities for weather and environmental monitoring, warning, and forecasting by four new instruments aboard FY-4A, i.e. Advanced Geosynchronous Radiation Imager (AGRI), the Geosynchronous Interferometric Infrared Sounder (GIIRS), the Lightning Mapping Imager (LMI), and the Space Environment Package (SEP). The navigation and registration is a key issue of the FY-4 ground segment for data application.

The navigation of AGRI data from geostationary three-axis stabilized satellite is a great challenge since it suffers from thermal elastic deformation. Thus, in order to compensate for

the changing deformation, it has to rely on stars for accurate navigation. Imagers aboard the three-axis stabilized Geostationary Operational Environmental Satellite (GOES) [4]–[6] routinely observe a selected set of stars for image navigation and registration. Star measurement utilizes the drift of the selected star moving across the field of view of the instrument's visible detectors, and it has been shown that separate and independent star sensing can increase the attitude precision of the optical axes of the imager and reduce the pointing error [4], [7], [8]. AGRI aboard FY-4A also observes stars at regular time intervals as a part of the operational process for image navigation and registration, and high precision of star centroiding is the first important issue in the process.

Star centroiding is to detect the accurate subpixel coordinates of the stars in star sensing images. It is the key issue for attitude determination of onboard three-axis stabilized spacecraft using star sensors/trackers. The precision of the star centroiding is an important factor affecting the performance of the star tracker [9]–[11]. To facilitate the subpixel precision of star centroiding, the optics of star sensor is usually out of focus slightly so that a star will occupy several pixels. Thus subpixel coordinates with high precision can be obtained by various centroid estimation methods. For example, Center of Mass (COM) method is popular to compute star centroid in a single star image [6], [9], [10] with advantage of simple principle and small amount of computing. [12] proposed a coaxial correlation method based on Gaussian function and [13] described a Fourier phase shifting method, both of which are more accurate. Most of these methods are based on a single frame with a complete star spot, and their precision is directly correlated to the size of the spot.

Different from star trackers, geostationary imagers like Imager of GOES [14], Advanced Himawari Imager (AHI) of Himawari-8 [15] and AGRI of FY-4A, are Earth observing sensors onboard, and usually focused to get high quality imagery products. While, a star appears as a point source in a focused image, and all its photoelectrons may be generated in a single pixel. This makes it difficult to calculate accurate subpixel coordinates of star centroids for focused sensors, and previous star centroiding methods for unfocused images may be out of action in the task of star sensing for navigation of satellite instruments. In addition, the detector columns of AGRI are actually separated between each others (as shown in Figure 1), resulting incomplete spots of the stars appeared in the images. It brings extra difficulty for accurate star centroiding for AGRI.

To solve the problems, this paper introduces a high precision star centroid extraction method for AGRI based on trajectory fitting and energy response curve fitting. Considering that AGRI abroad FY-4A performs continuous star sensing, we propose two different procedures for centroiding in north-south (Y) and east-west (X) directions due to the different properties of the detector array of AGRI in these two directions. For Y direction, we obtain a complete star trajectory across the field of view (FOV) of AGRI from whole image sequence and improve the coordinates of star centroids
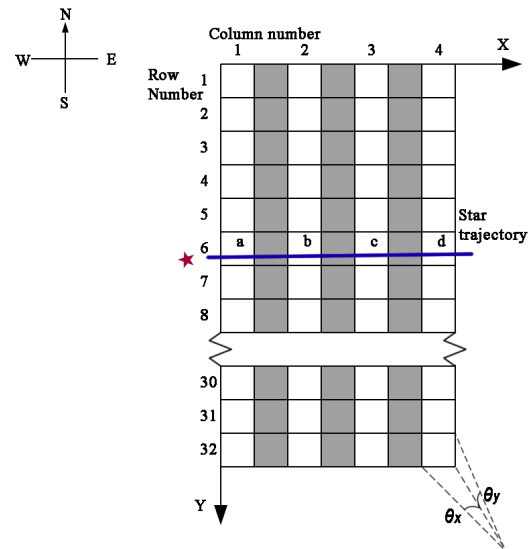

FIGURE 1. Detector array of AGRI aboard FY-4A and the example of it conducting a star look.

TABLE 1. Performance of AGRI onboard FY-4A.

Indicator	Parameter
Channels	14
Spatial Resolution (visible)	0.5-1 km
Spatial Resolution (near infrared)	2 km
Spatial Resolution (infrared)	4 km
Temporal Resolution	15min/full disk
Field of Observation	21°NS×23°EW and its subregion
Magnitude	6Mv
Navigation accuracy	1 infrared pixel

by projecting the subpixel coordinates calculated by COM method from each frame to the trajectory. For X direction, we find a Gaussian energy response curve of detectors where the star passes and calculate the accurate moments when the star crosses the center of the detectors in X direction. In addition, a new star detection method is also introduced in this paper, which has shown a good performance with strong robustness against noise. Experiments on simulated star images in various conditions show that our method can robustly calculate accurate subpixel coordinates of star centroids and significantly reduce the centroiding error. Results of in-orbit testing of FY-4A validate the feasibility and effectiveness of our method.

The rest of the paper is organized as follows. In Section II, we briefly introduce the properties of AGRI. Section III provides the details of our star centroiding method. Experimental results and analyses of the simulation and the in-orbit test are presented in Section IV and Section V respectively. Section VI concludes the paper.

II. OVERVIEW OF AGRI
AGRI is the primary payload of FY-4A, aiming to measure Earth environmental parameters such as land, ocean, cloud and atmosphere by means of high-precision and

TABLE 2. Spectral Configuration of AGRI onboard FY-4A.

No.	Central Band (μm)	Spectral Band (μm)	Spatial Resolution	Main Applications
1	0.47	0.45-0.49	1 km	aerosol, color image synthesis
2	0.65	0.55-0.75	0.5 km	vegetation, star sensing
3	0.825	0.75-0.90	1 km	vegetation, aerosol
4	1.375	1.36-1.39	2 km	cirrus
5	1.61	1.58-1.64	2 km	cloud, snow
6	2.225	2.10-2.35	2 km	cirrus, aerosol
7(a)	3.375	3.50-4.00	2 km	cloud, fire
7(b)	3.375	3.50-4.00	4 km	land surface
8	6.25	5.80-6.70	4 km	upper-level water vapor
9	6.95	6.75-7.15	4 km	mid-level water vapor
10	7.42	7.24-7.60	4 km	low-level water vapor
11	8.70	8.40-9.00	4 km	integrated water vapor, cloud
12	10.80	10.30-11.30	4 km	cloud, temperature
13	12.00	11.50-12.50	4 km	cloud, integrated water vapor, temperature
14	13.50	13.20-13.80	4 km	cloud, water vapor

multi-spectral quantitative remote sensing. AGRI can directly serve for weather analysis and forecasting, climate prediction, environment and disaster monitoring. Compared with Visible and Infrared Spin Scan Radiometer (VISSR) of FY-2, the latest generation of Fengyun series, AGRI has a better performance, with the advantage of more spectral channels, higher imaging frequency and higher spatial resolution [16].

A. PARAMETERS OF AGRI
Several important performance parameters of AGRI are shown in Table 1, and the information of its 14 channels is summarized in Table 2.

B. STAR SENSING OF AGRI
Star sensing is one of the main purpose of AGRI visible channel. Between Earth observations, two scan mirrors are used to point the line-of-sight (LOS) to certain preselected stars in the field of regard (FOR) [8]. Since FY-4A is a geostationary satellite with three-axis stabilized attitude, the LOS of AGRI rotates with a cycle of a sidereal day (23 hours 56 minutes 4 seconds) relative to the star field [5]. As a result, the selected stars pass though the detectors from the west to the east in turn.

Star sensing can be used for image navigation and registration (INR) by calculating the attitude of the payload with the difference between predicted star positions and the centroiding results of sensed star images. Compared with the INR methods based on landmark matching [8], star sensing has advantage of high precision and constant error, and can work in both day-time and night-time. In addition, a star is an ideal point source without the effect of atmosphere disturbance, from which LOS can be directly acquired. The second channel (0.55-0.75μm) of AGRI, as shown in Table 2, is used to scan stars at interval of Earth observations.

Figure 1 shows the layout of the detectors of AGRI for star sensing, which consists of four visible detector arrays. Between every two arrays, a gap exists with the same width as the detectors, causing incomplete star spot in X

direction. Each array is composed of 32 detectors with a 14 × 14 $\mu radians$ instantaneous filed of view (IFOV), as θ_x and θ_y in Figure 1. Thus, star images with a size of 32 × 4 in pixels, are captured by FY-4A and transferred to the ground station after star sensing. The blue line over the sixth row in Figure 1 shows an example trajectory of star centroid during star sensing, while the image of the star is reflected to the detectors via the two scan mirrors. The four detectors labeled $\{a, b, c, d\}$ in Figure 1 will have strong energy response when the star centroid is streaking across the four arrays. In the following of this paper, the star-passing detectors are called the *activated* detectors (e.g. $\{a, b, c, d\}$ in Figure 1) and the other detectors are called the *silent* ones.

III. STAR CENTROID DETECTION ALGORITHM
There are two great difficulties in the process of star centroid extraction. The first one is to detect star spots accurately in the star images, i.e. to distinguish them from noisy pixels. The second one is to extract star subpixel centroids in high precision. To solve the two problems above, a novel method is proposed as shown in Figure 2. First of all, a preprocessing method is used to remove both fixed and random noise in the star images and increase the signal to noise ratio (SNR). Then, the row number of the pixels where the star passes is determined according to the standard deviation of whole star scanning data. In addition, the column number of star region in each frame is detected according to the energy response curve. Finally, a star centroid extraction method based on energy curve fitting and trajectory fitting is used to calculate the high-precision centroids for X and Y directions respectively. The entire process is introduced in detail in the rest of this section.

A. STAR IMAGE PREPROCESSING
1) FIXED NOISE REMOVAL
Original star images contain strong fixed noise due to the sunlight and the reflection of the atmosphere, which makes it hard to detect star objective accurately. As shown in Figure 3(**a**), the star image is heavily impacted, causing the
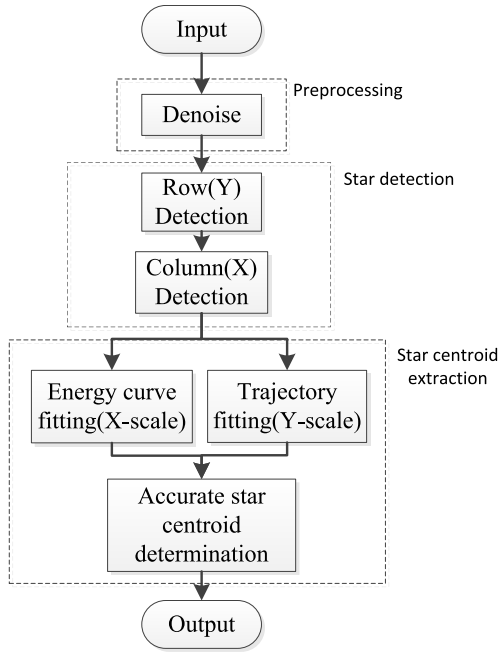
FIGURE 2. The flow chart of star centroid extraction method.

FIGURE 3. (a) An original single star image captured by AGRI in-orbit on June 20, 2017. (b) The star image after fixed noise removal.

FIGURE 4. A sequence of actual star images before (a) and after (b) fixed noise removal.

FIGURE 5. Amplitude-frequency response curve of the ideal low-pass filter, where F_c is the cut-off frequency.

pixels away from the true gray values of the star spot. Thus, we use the mean gray values of every pixel during the star scan to describe the fixed noise, and calculate the fixed noise as

$$I_n(x, y) = \frac{\sum_{k=1}^{N} I_k(x, y)}{N} \tag{1}$$

where $I_k(x, y)$ is k-th image of the sequence obtained during one time of continuous star scan, (x, y) denotes the coordinate of the pixel in the image, and N is the total number of the star images in the sequence. It should be noticed that the fixed noise $I_n(x, y)$ is of the same size as the star images $I_k(x, y), k = 1, \cdots, N$. To remove fixed noise, the fixed noise $I_n(x, y)$ is subtracted from each of the original images, and the actual energy response of the star remains, as shown in Figure 3(**b**).

In order to give a visual representation of a star sensing, the whole sequence of star images is reshaped into a single large image in column-major order, as shown in Figure 4(**a**), where a column of the large image with 128 pixels indicates one frame of star images and column numbers are the frame numbers in the original sequence. The data was generated at 00:28:30 June 20, 2017 (Universal Time Coordinated, UTC) by AGRI of FY-4A in orbit. The longitude and latitude of the observed star on the celestial sphere equal to 190.472 and 10.236 respectively, and the magnification of the star is 4.864. Figure 4(**b**) shows the result of fixed noise removal, of which the contrast and SNR are improved obviously.

2) RANDOM NOISE REMOVAL
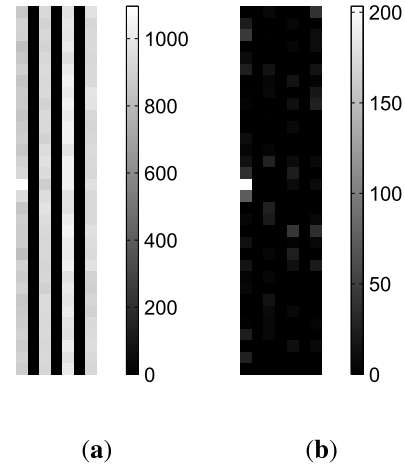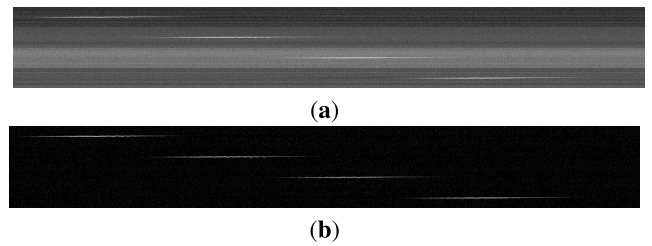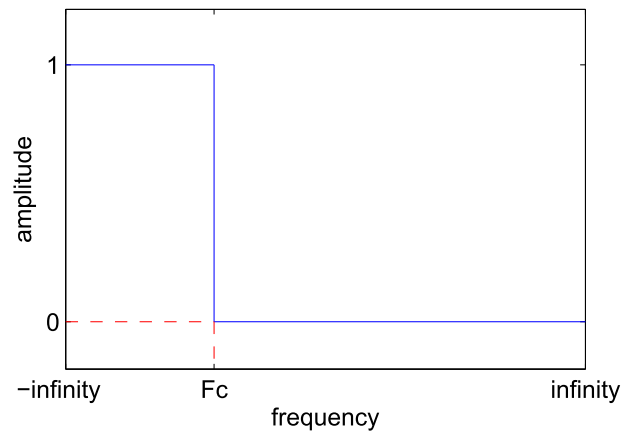Star images after fixed noise removal still have random noise (usually presented as singular points). Such singular points have great impact on the star detection. To reduce the influence of the singular points, the response curves of the 128 visible detectors are processed by an ideal low-pass digital filter

$$S_o = f_{LP}(S_i, F_s, F_c) \tag{2}$$

where S_i and S_o are the original signal and the treated signal, F_s represents the sampling frequency, and F_c is the cut-off frequency. Figure 5 is an illumination of the ideal low-pass digital filter. In practice, we convert the signal of every
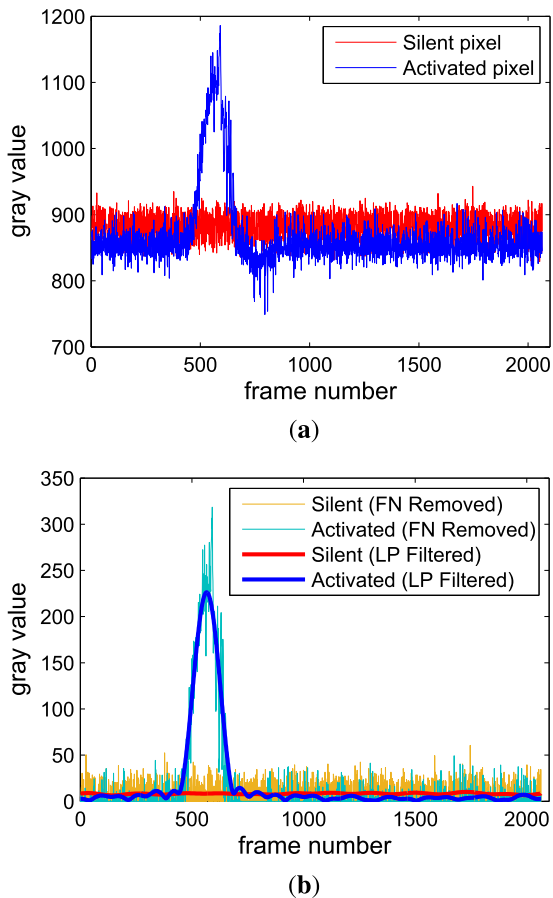
(a)

(b)

FIGURE 6. (a) The original signal of two detectors in the same column, where the blue line shows the star-passing detector, and the red line is the one without star passing. (b) The fixed noise (FN) removed and the low-pass (LP) filtered signals.

detector to the frequency domain by fast Fourier transform (FFT) [17] and apply a low-pass filter with the cut-off frequency $F_c = 3Hz$. Figure 6 shows the energy responding curve of a star-passing detector before and after low-pass filtering. It is clear that the random noise with high frequency has been suppressed by the low-pass filter, and the response of the star is preserved well. It should be noticed that the ideal low-pass filter used here can significantly suppress random noise in the star image without ringing artifacts (as shown in Figure 7), thus no other complex filter is needed in this case. Figure 7 shows the image sequence after random noise removal, where the four lines are corresponding to the star-passing detectors in the four arrays.

It is important to note that both fixed noise removal and random noise removal are used for star detection in Section III-B, while for the star centroiding process in Section III-C, only fixed-noise-removed images are used to avoid the detail change of the energy distribution around the star spots caused by the frequency-domain filter.

B. STAR DETECTION

The directions of the two scan mirrors keep fixed relative to the satellite during star scans, while the star steaks across the

FIGURE 7. Filtered star image sequence with ideal low-pass filter.

four detector arrays in a straight trajectory from the west to the east, due to the rotation of the satellite around the Earth (as mentioned in Section II-B). Theoretically, the trajectory goes horizontally crossing one row of the detectors, while the satellite keeps in the nominal attitude in geostationary orbit. However, because of the optical blur, more than one row could obtain response in different intensity when the star passes. Since AGRI is designed as a focal imager for the purpose of Earth observation, the size of the star spot is not larger than 3×3 (2×2 in most cases). As is shown in Figure 3(b), it is nearly impossible to differentiate star spots from noise pixels with only a single frame as a result of the similar features.

Star detection aims to establish the mapping relations between the pixels where the star centroid is located and the frame numbers. Our method separates the detection task into two sub-problems: responsive row detection and responsive column detection.

1) ROW DETECTION
Based on the horizontal trajectory of the sensed star, the star-passing row stands out for the strongest response relative to the other 31 rows. We calculate the mean gray values and the standard deviations of all the 128 detectors individually as shown in Figure 8. The mean values show the level of the visible detectors on average. The gray values of the star-passing detectors are higher than the others, with the four peaks represented in Figure 8(a). The row number can be figured out by taking the pixel number modulo 32, i.e. the length of a column. Similarly, as shown in Figure 8(b), the standard deviation can also be used to detect the activated row. According the statistics of one month star sensing data of AGRI aboard FY-4A, we find that the standard deviation has better stability in row detection than the mean value. Thus for better robustness, the standard deviation based method is used for row detection.

2) COLUMN DETECTION
The four detectors in the star-passing row are activated in turn from the west to the east during the star sensing. In other words, the star centroid moves from the 1st column to the 4th column as the responses of each column get peaks one after another. Thus, the column numbers of the star-passing detectors in every frames can be determined according to the energy response curves of each activated detector, shown as Figure 9. The four black crosses numbered $\{t_1, t_2, t_3, t_4\}$ represent the frames when the four star-passing pixels have the maximum response, corresponding to the moments when the star centroid is passing the centerline of an array in
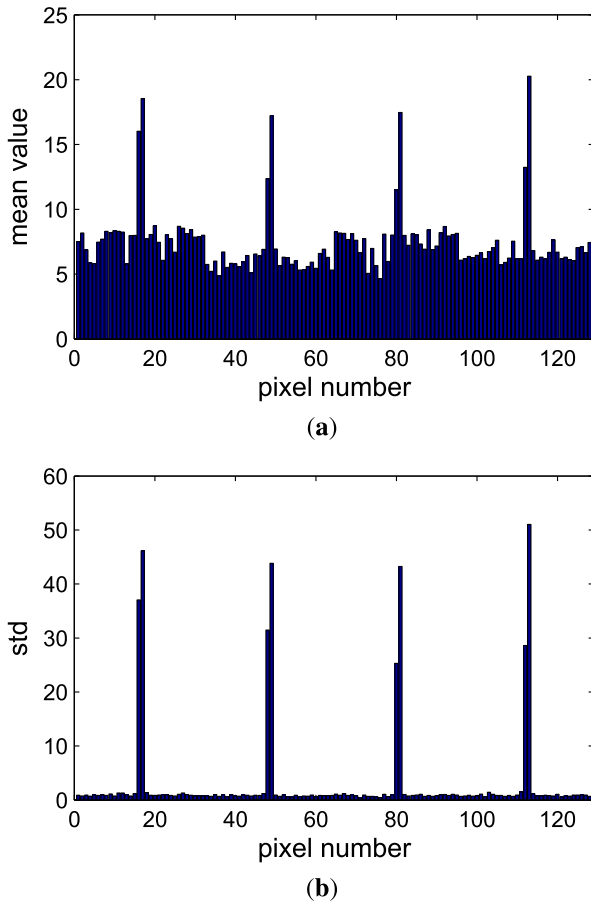
FIGURE 8. (a) Mean values of each detector. (b) Standard deviations (std) of each detector.

the frames. Depending on the intensity of the four response curves, the column numbers of the activated detectors can be determined in every frame, shown as the double-headed arrows in Figure 9.

To better calculate the centroid of the star, we consider a region with a size of 3×1 pixels to cover the distribution of star spot rather than a 3×3 region because of the gaps between detector arrays. The 3×1 region is determined according to the row and column detection, and the center pixel of the 3×1 region (called the main pixel) has the maximum energy response. Vast majority of star energy in each frame is distributed in the 3×1 region, which is used to calculate the subpixel coordinate of the star centroid in Section III-C.

C. STAR CENTROID EXTRACTION

The star energy distributed in each star image is discontinuous in X direction because of the gaps between detector arrays. However in Y direction, the raw subpixel Y coordinate can be estimated by the Center of Mass (COM) method in 3×1 regions. Thus, the high-precision coordinates of star centroid in X and Y directions are calculated based on energy curve fitting and trajectory fitting respectively.

1) HIGH-PRECISION X COORDINATE CALCULATION

Since the star can be regarded as an ideal point light source, the star spot in the star image can be seen as the point spread function (PSF) of AGRI. Due to the gaps between detector arrays, a part of the energy of the star spot loses. This makes it incapable to calculate the subpixel X coordinate of the star centroid only using a single star image. To solve the problem, we consider the energy distribution of the star in the focal plane (i.e. the PSF) approximatively as a two dimension Gaussian function [6], [9], [18], [19]

$$f(x, y) = \frac{1}{2\pi \sigma_{PSF}^2} \exp\left(-\frac{(x - \mu_x)^2 + (y - \mu_y)^2}{2\sigma_{PSF}^2}\right) \quad (3)$$

where σ_{PSF} is the standard deviation, controlling the width of the function, and μ_x and μ_y is the central position of the function. Therefore, the energy curve, i.e. the sum of gray values of a column, can be regarded as the double integral of Equation 3 as

$$g(x) = \int_{-\infty}^{\infty} \int_{x-0.5}^{x+0.5} f(x, y)\, dxdy$$
$$= \frac{1}{2}\left(\text{erfc}\left(\frac{x + 0.5 - \mu_x}{\sigma_{PSF}\sqrt{2}}\right) - \text{erfc}\left(\frac{x - 0.5 - \mu_x}{\sigma_{PSF}\sqrt{2}}\right)\right) \quad (4)$$

where $erfc(\cdot)$ is a non-elementary function [20] called Gaussian error function defined as

$$\text{erfc(x)} = \int_0^x \frac{2}{\sqrt{\pi}} e^{-t^2}\, dt \quad (5)$$

Noticing that $erfc(\cdot)$ cannot be described with an analytic expression, thus we use a Gaussian function $h(x)$ to fit $g(x)$ (Equation 4) approximately. $h(x)$ can be defined as

$$g(x) \approx h(x) = a \exp\left(-\left(\frac{x - b}{c}\right)^2\right) \quad (6)$$

Figure 10 shows the error between $g(x)$ and $h(x)$ with parameters $\mu_x = 0$, $\sigma_{PSF} = 1$ for $g(x)$ and $a = 0.383$, $b = 0$, $c = 1.473$ for $h(x)$. It can be seen that the curve of $h(x)$ is very close to that of $g(x)$ with a root-mean-square error (RMSE) of 6.676×10^{-5} (Figure 10(a)), and the error between $h(x)$ and $g(x)$ is always less than 2.0×10^{-4} (Figure 10(b)). This indicates the evidence in support of replacing $g(x)$ with $h(x)$.

Thus, the energy response curves of the four arrays can be described as four Gaussian functions peaking when the star centroid is at the centerline of array. Compared with the energy response curves calculated using the raw data (the original curves in Figure 11), Gaussian function is more accordant with the star energy distribution and can provide more accurate theoretical peaks with robustness. Considering that the X coordinate of the star spot can be linearly computed by its velocity v_0 and imaging time t, i.e. $x = v_0 t + x_0$, the target Gaussian function to be fitted can be

$$\hat{E}(t) = \hat{a} \exp\left(-\left(\hat{b}t - \hat{c}\right)^2\right) + \hat{d} \quad (7)$$
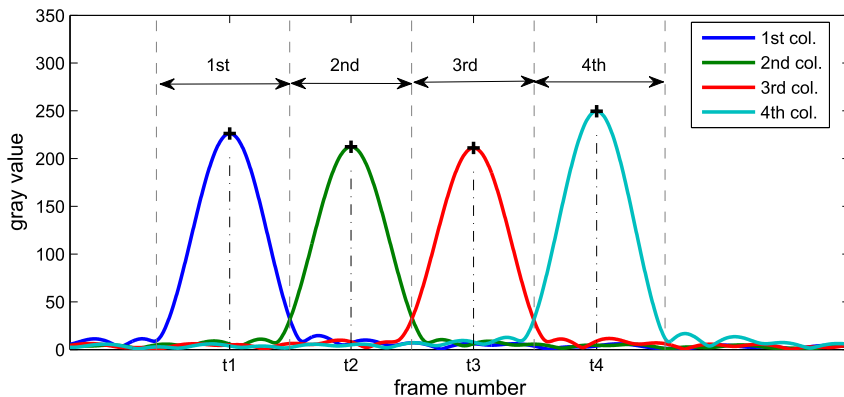
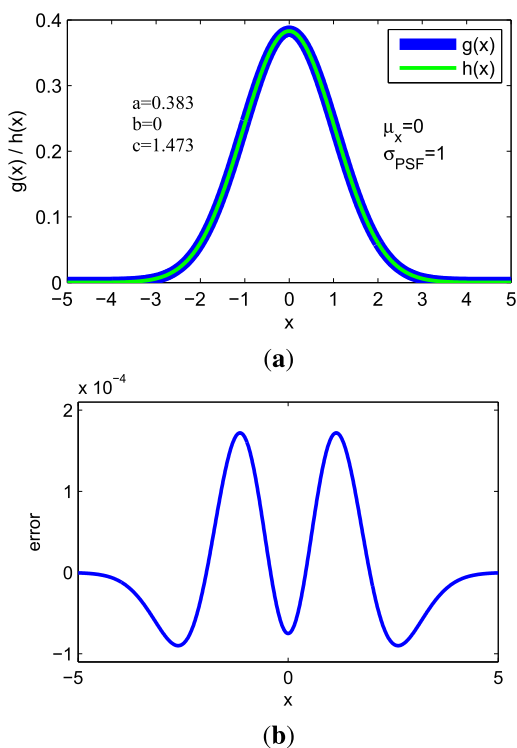**FIGURE 9.** The response curves of four activated detectors.

(a)

(b)

FIGURE 10. (a) The curve of *g(x)* and *h(x)*. (b) The error curve between *h(x)* and *g(x)*.

FIGURE 11. The results of the Gaussian curves fitted with LSF.

where $\hat{a}$ is the optimal estimation of a in Equation 6, $\hat{b}$ is the optimal estimation of v_0/c, $\hat{c}$ is the optimal estimation of $(b - x_0)/c$, and $\hat{d}$ is a bias parameter to model the residual noise for purpose of getting better Gaussian function fitting precision. The velocity $v_0 = 5.1944\ pixel/sec$ can be computed as Equation 14.

Given a sequence of star images $\{I_k\}, k = 1, \cdots, N$ captured at the time $\{t_k\}, k = 1, \cdots, N$, the observed value of Equation 7 can be calculated as
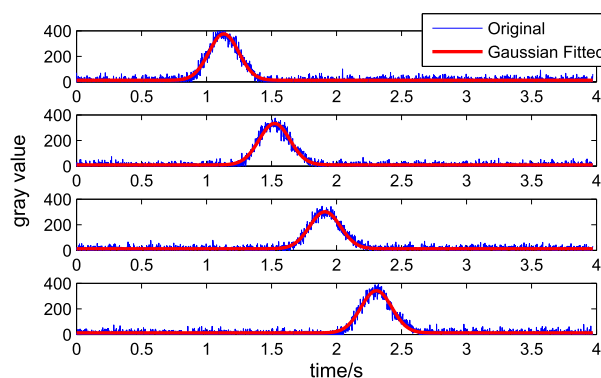
$$E_k = \sum_{y=y_c-1}^{y_c+1} I_k(x_c, y) \tag{8}$$

where (x_c, y_c) is the coordinate of the main pixel in the k-th star image. Compared with Equation 4, the integral operation from Negative Infinity to Positive Infinity is replaced with the sum of the three pixel centered on the main pixel since most star energy falls into a 3×1 region around the main pixel as mentioned at the end of Section III-B2. Then, the parameters of Equation 7 can be calculated with least square fitting (LSF) [21] as

$$\arg\min\left(\sum \frac{1}{2}(E_k - \hat{E}(t_k))^2\right) \tag{9}$$

Figure 11 shows the results of the Gaussian curves fitted with LSF method. The four peaks are the positions when the star centroid is at the centerline of an array. In other words, the X coordinates of the star centroid equal to $\{0.5, 2.5, 4.5, 6.5\}$ at the peaks of the fitted Gaussian curves. According to Equation 7, the exact peaking moments $\{t_1, t_2, t_3, t_4\}$ can be calculated as

$$t_j = \frac{\hat{c}_j}{\hat{b}_j} \quad j = 1, \ldots, 4 \tag{10}$$

where $\hat{b}_j$ and $\hat{c}_j$ are the parameters of Equation 7 for the j-th detector array. The X coordinates of the star spot in each frame can be obtained by fitting the linear function $x = v_0 t + x_0$ by LSF using the data at four peaks.
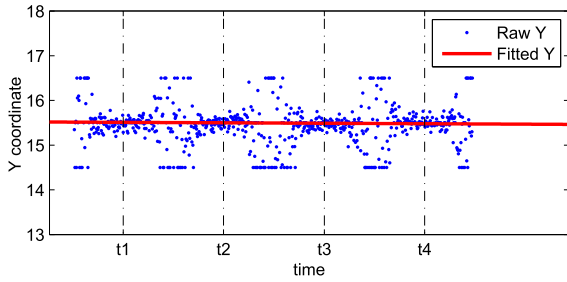
FIGURE 12. The result of the Y coordinates calculated with LSF.

2) HIGH-PRECISION Y COORDINATE CALCULATION

As shown in Figure 1, the detectors are placed tightly in Y direction. Thus, the raw Y coordinate of the star centroid in a single frame $I_k(x, y)$ can be calculated using Center of Mass (COM) method [9] as

$$Y_k = \frac{\sum_{y=-1+y_c}^{1+y_c} y I_k(x, y)}{\sum_{y=-1+y_c}^{1+y_c} I_k(x, y)} \tag{11}$$

where y_c is the row number of the main pixel. However, the raw Y coordinates calculated with COM method is in error because of the remaining noise in star images. Considering the star trajectory on the focal plane, we can reduce the error by fitting the linear trajectory by LSF using the the raw Y coordinates.

Figure 12 shows the result of LSF method for Y coordinate calculation, where the blue dots are the raw Y coordinates calculated with COM method in every frame, and the red line is the fitted line of LSF. The four chain lines marked with t_1, t_2, t_3, t_4 represent the moments when the star centroid is at the centerline of a detector array. We call t_1, t_2, t_3, t_4 the column-center moments in this paper.

It can be seen from Figure 12 that the raw Y coordinates of the frames close to the column-center moments are more stable with less centroiding error. In theory, the energy is more concentrated when the star centroid is close to the center of a pixel. Therefore, the precision of the raw Y coordinates near the column-center moments is less influenced than that of other coordinates in the same noise level. Thus the LSF method can be optimized as weighted least square fitting (WLSF) method to minimize the weighted sum of square errors between predicted coordinates $\hat{Y}$ and measured coordinates Y, i.e.

$$\arg\min \left(\sum \frac{1}{2} W_k (Y_k - \hat{Y}_k)^2 \right) \tag{12}$$

The weight W_k is calculated with the distance of the location of the star centroid to the center of an array as

$$W_k = \begin{cases} f(v_0 \cdot \Delta t_k) & f(v_0 \cdot \Delta t_k) \geq 0 \\ 0 & f(v_0 \cdot \Delta t_k) < 0 \end{cases} \tag{13}$$

where $f(\cdot)$ is the weight function to reduce the influence of the values away from the centerline of an array on the Y coordinate calculation, Δt_k is the interval from the imaging moment
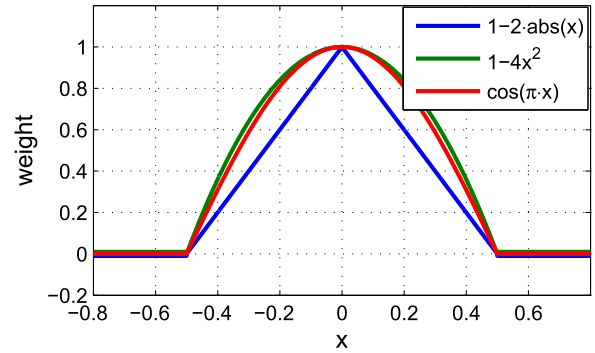

FIGURE 13. Three curves describe the linear ($f(x) = 1 - 2 \cdot abs(x)$), quadratic ($f(x) = 1 - 4x^2$) and cosine ($f(x) = \cos(\pi x)$) functions.

of the k-th star image to the nearest column-center moment, and v_0 is the velocity of the star centroid shifting on the image. Since FY-4A is a three-axis stabilized geostationary satellite, v_0 can be calculated as

$$v_0 = \frac{2\pi}{\zeta} \cdot \frac{1}{\psi} = 5.1944 \ pixel/sec \tag{14}$$

where $\zeta = 23h \ 56min \ 4sec$ (*sidereal day*) is the orbital period of FY-4A, and $\psi = 14\mu rad/pixel$ is the angular resolution of a detector. In this paper, we consider three types of $f(\cdot)$ including linear, quadratic and cosine functions as shown in Figure 13.

IV. SIMULATION EXPERIMENTS

Since the true subpixel coordinates of the star centroid cannot be obtained during the satellite working in orbit, the performance of our method is firstly evaluated using simulated data.

A. STAR IMAGE SIMULATION

To simulate the actual imaging condition, pin-hole camera model is adopted, in which stars are projected onto the focal plane through the aperture. 2D Gaussian PSF [6], [9], [19] is used to model the optical characteristic of a star as a point light source. The integral manner of PSF for reasonable sampling of the Gaussian energy distribution is used as in [19]. The base gray value of each detector is set to 150 in order to model the reflection of the sunlight. The entire energy of the star spot is set to 250, distributed in the region of several pixels according to the PSF. The velocity of the star centroid is set to 5.1944 pixel/sec and the frame frequency is set to 500Hz. 1000 frames are generated in each sequence. It should be noticed that all these parameters are chosen according to the actual performance of AGRI for star sensing.

For simulation experiments, we simulate two subsets of data to analyze the main factors impacting star centroiding, including the random noise, the initial Y coordinate when the star comes into the IFOV, and the width of Gaussian PSF.

1) NOISY SUBSET

In this subset, the initial Y coordinate is firstly set from 16.00 to 16.99, with a step of 0.01 pixels, to simulate the
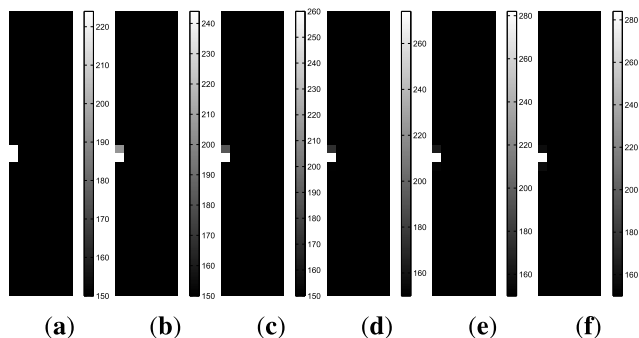
FIGURE 14. Simulated noise-free frames of star images with the initial Y coordinate of (a) 0.00, (b) 0.10, (c) 0.20, (d) 0.30, (e) 0.40, and (f) 0.50. Those with the initial Y coordinates from 0.60 to 0.90 are omitted because of the symmetry of 2D Gaussian PSF.
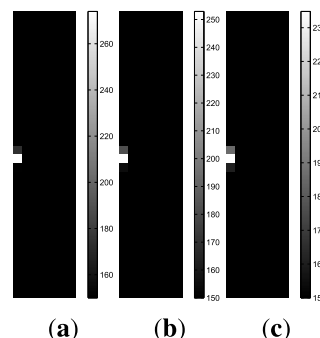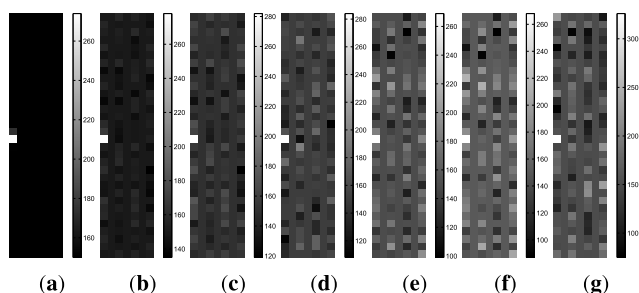

FIGURE 15. Simulated frames of star images in different noise level, with σ_n of (a) 0, (b) 5, (c) 10, (d) 15, (e) 20, (f) 25, and (g) 30.

FIGURE 16. Simulated noise-free frames of star images with σ_{PSF} of (a) 0.3, (b) 0.4, and (c) 0.5.
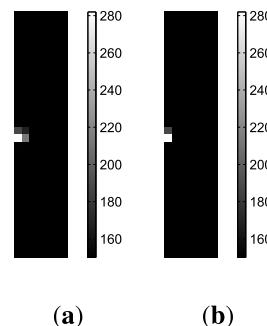

FIGURE 17. Simulated noise-free frames of star images, with (a) and without (b) gaps between arrays. The star centroid coordinates of the two images are both (0.860, 16.232).

influence on the distribution of the star energy in Y direction. Then, a zero mean white Gaussian noise is used to model the noise in the simulated star images, the standard deviation (σ_n) of which is set from 0 to 30 with a step of 5. Images in this subset are simulated with the Gaussian PSF of $\sigma_{PSF} = 0.3$. Several simulated images with different initial Y coordinates of the star centroid are shown in Figure 14. Figure 15 shows the single frames in different noise levels. For better visualization, the three columns of gaps are filled with 150 (the base gray value of the images).

2) GAUSSIAN PSF SUBSET
In this subset, the standard deviation of the Gaussian PSF (σ_{PSF}) is set from 0.3 to 0.5 pixels to simulate the different focused imaging modes. Gaussian noise is also added with the standard deviation (σ_n) from 0 to 30 with a step of 5. Figure 16 shows the sample images with different width of Gaussian PSFs.

B. THE IMPACT OF THE GAPS ON COM METHOD
To analyze the impact of the gaps of AGRI for sub-pixel star centroiding, we simulate star images with and without gaps (Figure 17) and report single-frame centroiding results of the popular Center of Mass (COM) method in Table 3. As is shown in Table 3, the X errors of COM method are all close to 0.5 pixels when there are gaps between detector arrays. It is nearly impossible to calculate accurate subpixel X

coordinates with COM method due to the gaps. For Y direction, the gaps make little impact on the precision of subpixel coordinates, that is why COM is selected to calculate the raw Y coordinate of the star centroid in a single frame as mentioned in Section III-C2.

C. PERFORMANCE OF STAR DETECTION
We compare our star detection method with Region Growing (RG) [22], a common segmentation method used for target detection. Preprocessing including fixed noise removal and low-pass filtering is applied before star detection. Table 4 shows the comparison results on the noisy subset under different standard deviation of Gaussian noise (σ_n).

It can be seen from Table 4 that the precision of RG method is severely affected by the noise of the star images. RG does not work well in the aspect of recall ratio, either. By contrast, our detection method achieves 100% precision and is robust against noise. This is because our method considers the ensemble feature of the entire sequence of star images. The recall ratio of our method is only 92.89%, which means that 7.11% stars are missed. The reason is that we detect column locations of the star centroid according to the intensity of the response curves as mentioned in Section III-B2, and drop the regions far from the peaks of the curves i.e. where the star centroid is in the gaps between the detector arrays. In these cases, the star energy of those regions is almost zero,

TABLE 3. The impact of the gaps to the error of COM method (pixel).

		$\sigma_n =0$	$\sigma_n =5$	$\sigma_n =10$	$\sigma_n =15$	$\sigma_n =20$	$\sigma_n =25$	$\sigma_n =30$
Gaps	X	0.4987	0.4987	0.4987	0.4987	0.4987	0.4987	0.4988
	Y	0.1369	0.1631	0.1803	0.1966	0.2125	0.2268	0.2362
No Gaps	X	0.1423	0.1485	0.1636	0.1834	0.2043	0.2199	0.2259
	Y	0.1226	0.1300	0.1482	0.1717	0.1968	0.2177	0.2302

TABLE 4. Precision (ϵ_p) and recall (ϵ_r) for star detection.

Method	Indicator	$\sigma_n =0$	$\sigma_n =5$	$\sigma_n =10$	$\sigma_n =15$	$\sigma_n =20$	$\sigma_n =25$	$\sigma_n =30$
RG	ϵ_p	97.09%	65.94%	58.83%	68.83%	75.34%	77.43%	74.29%
	ϵ_r	89.11%	77.63%	86.85%	88.48%	88.60%	87.92%	86.99%
Ours	ϵ_p	100.00%	100.00%	100.00%	100.00%	100.00%	100.00%	100.00%
	ϵ_r	92.89%	92.89%	92.89%	92.89%	92.89%	92.89%	92.89%

TABLE 5. Performance comparison on centroiding error of COM and our method (pixel).

		$\sigma_n =0$	$\sigma_n =5$	$\sigma_n =10$	$\sigma_n =15$	$\sigma_n =20$	$\sigma_n =25$	$\sigma_n =30$
COM	X	0.4987	0.4987	0.4987	0.4987	0.4987	0.4987	0.4988
	Y	0.1369	0.1631	0.1803	0.1966	0.2125	0.2268	0.2362
Ours	X	0.0005	0.0017	0.0031	0.0047	0.0061	0.0082	0.0095
	Y	0.0397	0.0487	0.0613	0.0747	0.0874	0.1001	0.1095

hidden in the background. By dropping these regions, we can guarantee the precision of centroiding.

D. PERFORMANCE OF CENTROID EXTRACTION

To quantitatively validate the precision of our centroid extraction method, we perform comparison with the popular centroiding method COM on the noisy subset, and the experimental results are shown in Table 5. Cosine function is used as the weight function for Y coordinate calculation.

From Table 5, it can be concluded that our centroiding method achieves quite higher precision in different noise levels. Taking full advantage of star sensing with high imaging frequency, our energy curve fitting method achieves really high precision. Especially for X coordinates, the accuracy of our method is improved by almost three orders of magnitude. By contrast, COM method is nearly invalid to calculate the subpixel X coordinate for AGRI star images due to the incomplete star spots. Meanwhile, the precision of Y coordinates extracted by our method is also significantly improved more than 50% comparing with that of COM.

E. ROBUSTNESS AGAINST NOISE AND MANTISSA OF INITIAL Y COORDINATES

The energy distribution in the star region is influenced by Y coordinates of the star centroid and random noise in the image. We evaluate the performance of our method under different mantissa of the initial Y coordinate of the star trajectory and different noise levels on the noisy subset.

The curves in Figure 18 represent the centroiding errors under different noise levels with the standard deviation σ_n from 0 to 30. We can see that the noise is one of the major factors effecting the centroiding precision and the
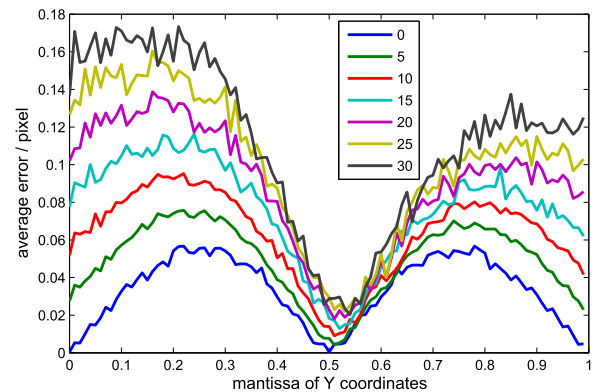

FIGURE 18. Error of our method under different mantissa of the initial Y coordinate. The legends indicate the the standard deviation σ_n of Gaussian random noise.

influence strengthens as the standard deviation of Gaussian noise increases. Meanwhile, it is clear that the centroiding precision of our method is obviously influenced by the mantissa of Y coordinate of the trajectory and such influence weakens when the mantissa of initial Y coordinate is around 0.5 i.e. the star centroid passes nearly through the centerline of a detector raw. It is because the energy of the star almost entirely falls into a single detector in this case. The second best centroiding precision appears across the border between two detector rows, i.e. the mantissa of initial Y coordinate is near 0 or 1, since the energy of the star captured by two detectors of neighbor rows is approximately equal and intact. The worst situation appears around a quarter of a detector, where the energy distributes the most unevenly in Y direction. Therefore, a star sensing with the trajectory passes the center of a detector or the border between two detectors is highly preferred in actual application.

TABLE 6. Error of our method under different width of PSF (pixel).

		$\sigma_n = 0$	$\sigma_n = 5$	$\sigma_n = 10$	$\sigma_n = 15$	$\sigma_n = 20$	$\sigma_n = 25$	$\sigma_n = 30$
σ_{PSF}=0.3	X	0.0004	0.0017	0.0032	0.0047	0.0063	0.0078	0.0095
	Y	0.0346	0.0488	0.0633	0.0754	0.0872	0.0992	0.1108
σ_{PSF}=0.4	X	0.0004	0.0022	0.0042	0.0061	0.0080	0.0102	0.0127
	Y	0.0107	0.0231	0.0380	0.0539	0.0691	0.0833	0.0964
σ_{PSF}=0.5	X	0.0005	0.0028	0.0053	0.0080	0.0106	0.0136	0.0159
	Y	0.0130	0.0248	0.0397	0.0574	0.0732	0.0913	0.1056

TABLE 7. Error of Y coordinates with different weight functions (pixel).

Weight function	$\sigma_n = 0$	$\sigma_n = 5$	$\sigma_n = 10$	$\sigma_n = 15$	$\sigma_n = 20$	$\sigma_n = 25$	$\sigma_n = 30$
Constant 1	0.0348	0.0582	0.0782	0.0962	0.1131	0.1297	0.1443
Linear	0.0347	0.0505	0.0666	0.0802	0.0930	0.1054	0.1182
Quadratic	0.0346	0.0490	0.0637	0.0761	0.0881	0.1002	0.1122
Cosine	0.0346	0.0489	0.0636	0.0758	0.0878	0.1000	0.1119

F. INFLUENCE OF THE WIDTH OF PSF

It is well known that the distribution of star energy has an important impact on star centroiding. We change the width of Gaussian PSF, controlled by the standard deviation σ_{PSF}, to simulate the changing of the energy distribution. Experiments has been performed on the Gaussian PSF subset to analyze the influence of the width of PSF on our proposed method. Table 6 shows the centroiding precision under different σ_{PSF}. It indicates that larger width of PSF (e.g. $\sigma_{PSF} = 0.4$) is beneficial to the centroiding precision. However, the precision is reduced slightly when the value of σ_{PSF} reaches 0.5 pixel. It is because our method is designed for focal imagers, and 3×1 regions are selected to cover the distribution of star energy of AGRI. As a result, the 3×1 regions cannot cover the entire star spots of a Gaussian PSF with a large width.

G. THE ROLE OF WEIGHT FUNCTIONS

We use weighted least square fitting (WLSF) for high-precision Y coordinate calculation. We test three kinds of weight functions including linear, quadratic and cosine, as shown in Figure 13. The traditional LSF method (i.e. the weight of each square error is constantly one) is regarded as the baseline for comparison. The results reported in Table 7 show that the centroiding precision is remarkably improved depending on the weight functions, especially under high noise levels. WLSF gives prominence to the raw coordinates close to the centerlines of the visible arrays, which contributes to the suppression of the noise impact. Cosine function performs the best and is selected to achieve other experiments in this paper.

V. IN-ORBIT TESTING RESULTS

Since the launch of FY-4A on December 11, 2016, the proposed star centroiding method has been tested for over 10 months in actual tasks, showing good effectiveness and robustness for accurate star centroid detection for AGRI aboard Fengyun-4A. Some example results of the in-orbit experiments are introduced in this section.

TABLE 8. The execution success ratio of our method.

Date	Non-midnight	Midnight (Local time 22:00-02:00)
2017/09/20	99.64%	43.24%
2017/09/21	99.64%	48.33%
2017/09/22	99.29%	50.43%
2017/09/23	99.73%	50.00%
2017/09/24	99.64%	47.01%
2017/09/25	99.38%	46.15%
Average	99.55%	47.53%

A. EFFECTIVENESS OF STAR CENTROIDING

To evaluate the effectiveness of our star centroiding method for in-orbit testing, we define the execution success ratio as

$$r_s = \frac{N_s}{N_e} \times 100\% \tag{15}$$

where N_s is the number of star sensing tasks that successfully detect the star regions and simultaneously calculate the correct subpixel coordinates, and N_e is the entire number of star sensing tasks during a certain period.

Table 8 shows the execution success ratio of our star centroiding method during the in-orbit test of FY-4A from 2017/09/20 to 2017/09/25 (UTC). Totally, centroiding results of 7441 times of star sensing tasks are involved in the analysis.

As shown in Figure 8, our method achieves good performance in most star sensing tasks expecting midnight, with the success ratio near 100%. However, the average execution success ratio of the star sensing tasks in the 4 hours around local time 0 o'clock (22:00-02:00) is only about 47.53%. The reason is that the line-of-sight of AGRI is close to the Sun at midnight due to the geostationary orbit of FY-4A. At this time, the star images suffer from the reflection of sunlight. The resulted problems including strong background noise and image saturation make the failure of star centroiding.

B. PRECISION OF STAR CENTROIDING

To quantitatively evaluate the precision of our centroiding method during the in-orbit test, we manually label the star centroid coordinates of the actual star sensing images frame

TABLE 9. Error of our method in actual observation data of AGRI.

Error/pixel	Image amount	Percentage	Subtotal
0.00-0.05	316	35.35%	35.35%
0.05-0.10	222	24.83%	60.18%
0.10-0.15	136	15.21%	75.39%
0.15-0.20	106	11.86%	87.25%
0.20-0.25	71	7.94%	95.19%
0.25-0.30	32	3.58%	98.77%
≥ 0.30	11	1.23%	100.00%
Total	**894**	**100%**	–

by frame as the ground truth for error computation. Firstly, the patches of 5×5 pixels centered on the main pixels are enlarged 100 times by nearest-neighbor interpolation. Then we mark the subpixel coordinates of the star centroids according to the energy distribution in the enlarged patches by visual observation. Total 894 images of star sensing tasks achieved by AGRI aboard FY-4A on September 23, 2017 are used for quantitative evaluation, and the results are shown in Table 9. The precision of 98.77% images is better than 0.30 pixels according to visually labeled ground truth, and over 87% errors are less than 0.20 pixels. It can be validated that our method achieves high precision of star centroiding in actual in-orbit data.

VI. CONCLUSIONS

In this paper, a star centroid extraction method has been specially designed for AGRI of FY-4A. For north-south (Y) direction, a complete star trajectory is fitted using WLSF, and the coordinates of star centers are improved by projecting the COM coordinates to the trajectory. For east-west (X) direction, Gaussian energy response curves of each detector array are fitted to get accurate peaks when the star passes the centers of the detector arrays. Our method overcomes the difficulty that the gaps between the columns of AGRI detectors make it nearly impossible to extract star centroid in subpixel. The quantitative precision validated by simulation experiments is better than 0.12 pixels in the images with the noise standard deviation of 30. Robustness analysis has also been performed on simulated datasets in different conditions. In addition, our method is sufficiently tested during the in-orbit test of FY-4A over 10 months, playing an significant role in the high-precision image navigation of FY-4A. The precision of our method for actual images by visual comparison is better than 0.30 pixels for most data.

REFERENCES

[1] J. Yang, "Development and applications of China's Fengyun (FY) meteorological satellite," *Spacecraft Eng.*, vol. 17, no. 3, pp. 23–28, May 2008.

[2] S. I. Rani, D. Srinivas, and J. P. George, "A review of the space based remote sensing for NWP," *Proc. SPIE*, vol. 9876, p. 98762H, May 2016.

[3] J. Yang, Z. Zhang, C. Wei, F. Lu, and Q. Guo, " Introducing the new generation of Chinese geostationary weather satellites, Fengyun-4," *Bull. Amer. Meteorol. Soc.*, vol. 98, no. 8, pp. 1637–1658, Aug. 2017.

[4] A. A. Kamel, "GOES image navigation and registration system," *Proc. SPIE*, vol. 2812, pp. 766–777, Oct. 1996.

[5] J. C. Bremer, J. G. Baucom, H. V. Vu, M. P. Weinreb, and N. Pinkine, "Estimation of long-term throughput degradation of GOES 8 and 9 visible channels by statistical analysis of star measurements," *Proc. SPIE*, vol. 3439, pp. 145–155, Oct. 1998.

[6] S. Özkan, E. Tola, and M. Soysal, "Performance of star centroiding methods under near-real sensor artifact simulation," in *Proc. 7th Int. Conf. Recent Adv. Space Technol. (RAST)*, Jun. 2015, pp. 615–619.

[7] G. Qiang and X. Di, "On-orbit modification of pointing error for imager in geostationary satellite based on star sensing," *Acta Opt. Sinica*, vol. 29, no. 9, pp. 2413–2420, Sep. 2009.

[8] L. I. Xiao-Kun, G.-Q. Wang, and G.-L. Chen, "FY-4 imager: Visible channel star sensing," *Sci. Technol. Eng.*, vol. 7, no. 6, pp. 993–996, 2007.

[9] C. C. Liebe, "Accuracy performance of star trackers—A tutorial," *IEEE Trans. Aerosp. Electron. Syst.*, vol. 38, no. 2, pp. 587–599, Apr. 2002.

[10] J. Yang, B. Liang, T. Zhang, and J. Song, "A novel systematic error compensation algorithm based on least squares support vector regression for star sensor image centroid estimation," *Sensors*, vol. 11, no. 8, pp. 7341–7363, 2011.

[11] X. Wang, X. Wei, Q. Fan, J. Li, and G. Wang, "Hardware implementation of fast and robust star centroid extraction with low resource cost," *IEEE Sensors J.*, vol. 15, no. 9, pp. 4857–4865, Sep. 2015.

[12] P. Seitz, "Optical superresolution using solid-state cameras and digita; signal processing," *Opt. Eng.*, vol. 27, no. 7, p. 277535, 1988.

[13] J.-P. Fillard, "Sub-pixel accuracy location estimation from digital signals," *Opt. Eng.*, vol. 31, no. 11, pp. 2465–2471, 1992.

[14] L. Wang, X. Wu, F. Weng, and M. D. Goldberg, "Effects of ice decontamination on GOES-12 imager calibration," *IEEE Trans. Geosci. Remote Sens.*, vol. 51, no. 3, pp. 1224–1230, Mar. 2013.

[15] F. Yu, X. Wu, X. Shao, and V. Kondratovich, "Evaluation of Himawari-8 AHI geospatial calibration accuracy using SNPP VIIRS SNO data," in *Proc. Geosci. Remote Sens. Symp.*, Jul. 2016, pp. 2925–2928.

[16] F. Lu and Y. Shou, "Channel simulation for FY-4 AGRI," in *Proc. Geosci. Remote Sens. Symp.*, Jul. 2011, pp. 3265–3268.

[17] C. Van Loan, *Computational Frameworks for the Fast Fourier Transform.* Beijing, China: Tsinghua Univ. Press, 2011.

[18] J. Yang, Z. Tao, J.-Y. Song, and H.-L. Zhu, "A new sub-pixel subdivision location algorithm for star image," in *Proc. Int. Congr. Image Signal Process.*, Oct. 2009, pp. 1–5.

[19] H. Wang, Y. Wang, L. Zhifeng, and S. Zhenfei, "Systematic centroid error compensation for the simple Gaussian PSF in an electronic star map simulator," *Chin. J. Aeronautics*, vol. 27, no. 4, pp. 884–891, Aug. 2014.

[20] S.-H. Chang, P. C. Cosman, and L. B. Milstein, "Chernoff-type bounds for the Gaussian error function," *IEEE Trans. Commun.*, vol. 59, no. 11, pp. 2939–2944, Nov. 2011.

[21] D. York, "Least squares fitting of a straight line with correlated errors," *Earth Planetary Sci. Lett.*, vol. 5, pp. 320–324, Jan. 1969.

[22] R. Adams and L. Bischof, "Seeded region growing," *IEEE Trans. Pattern Anal. Mach. Intell.*, vol. 16, no. 6, pp. 641–647, Jun. 1994.
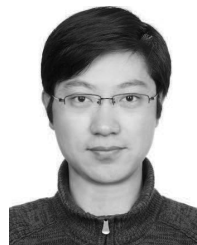
HAOPENG ZHANG (M'14) received the B.S. and Ph.D. degrees from Beihang University, Beijing, China, in 2008 and 2014, respectively. He is currently an Assistant Professor at the Image Processing Center, School of Astronautics, Beihang University. His main research interests include remote sensing image processing, multi-view object recognition, 3-D object recognition and pose estimation, and other related areas in pattern recognition, computer vision, and machine learning.
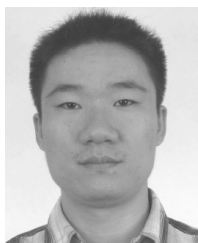
YI SU received the B.S. degree from Beihang University, Beijing, China, in 2016, where he is currently working toward the M.S. degree at the Image Processing Center, School of Astronautics. His research interests include computer vision and pattern recognition.
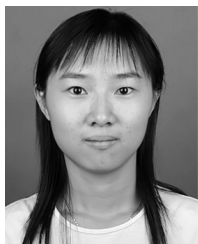
JIAN SHANG received the Ph.D. degree in communication and information system from the Institute of Electronics, Chinese Academy of Sciences, Beijing, China, in 2009. She is currently with the National Satellite Meteorological Center, China Meteorological Administration. Her research interests include remote sensing information processing and remote sensing instrument design.
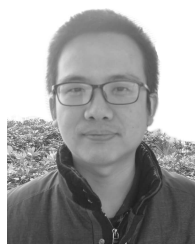
LEI YANG received the B.S. and M.S. degrees in applied mathematics from Northeastern University, China, in 2000 and 2003, respectively, and the Ph.D. degree in pattern recognition and intelligent systems from the Institute of Automation, Chinese Academy of Sciences, in 2006. He is currently a Professor at the National Satellite Meteorological Center, China Meteorological Administration. His current research interests include system design and implementation on image navigation and registration for China next-generation meteorological satellites.

BOWEN CAI received the B.S. degree in computer science and technology from the Jilin University of Finance and Economics, Changchun, China, in 2013. He is currently working toward the Ph.D. degree at the Image Processing Center, School of Astronautics, Beihang University, Beijing, China. His current research interests include machine learning, pattern recognition, and computer vision in remote sensing applications.

CHENGBAO LIU received the Ph.D. degree from the University of Chinese Academy of Sciences in 2013. He is currently with the National Satellite Meteorological Center, China Meteorological Administration. His main research is on the geolocation algorithm for the remote sensing data of Chinese meteorological satellites.
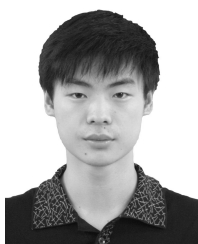
JING WANG received the Ph.D. degree in optical engineering from the Beijing Institute of Technology in 2015. She is currently with the National Satellite Meteorological Center, China Meteorological Administration. Her current research interests include implementation on image navigation for China meteorological satellites.

SHENGXIONG ZHOU received the B.S. degree from Wuhan University, Wuhan, China, in 2004. He currently with the Southwest Electrics and Telecommunication Technology Research Institute. His research interests include image positioning, data processing, and system architecture design.

ZHIQING ZHANG received the B.S. degree in radio engineering from Northeastern University, China, in 1986. He is currently a Professor of senior engineer and a Chief Designer at the National Satellite Meteorological Center, China. His current research interests include system design and implementation on ground segment and application system for China geostationary meteorological satellite.

● ● ●